ER-Localized Ceramide Accumulation Due to Disrupted CERT Transport Contributes to Replicative Senescence

Shweta Chitkara[1], Natasha Gozali[1], Andrey Kuzmin[1], Artem Pliss[2], Paras Prasad[1], Yasemin Sancak[3], G. Ekin Atilla-Gokcumen[1]*.

[1]Department of Chemistry, University at Buffalo, The State University of New York, Buffalo, New York 14260, USA

[2]School of Pharmacy, D'Youville University, Buffalo, New York 14201

[3] Department of Pharmacology, University of Washington, Seattle, WA

*Corresponding author: ekinatil@buffalo.edu (G. Ekin Atilla-Gokcumen)

ABSTRACT

Ceramides are bioactive sphingolipids that are central to cellular metabolism, signaling, and stress responses. Synthesized *de novo* in the endoplasmic reticulum (ER) through a tightly regulated enzymatic pathway, ceramides can also be generated from hydrolysis complex sphingolipids, including hexosylceramides and sphingomyelins, and the salvage pathway. Their dynamic turnover across distinct cellular compartments results in spatial regulation of ceramide levels and its functional consequences. Mitochondrial ceramide accumulation, in particular, is a critical factor of apoptosis, where ceramides can disrupt membrane integrity. In addition to apoptosis, ceramides are implicated in replicative senescence. However, the mechanisms of ceramide regulation and function in senescence remain incompletely understood. In this study, we employed comparative lipid profiling, gene expression analysis and Raman spectroscopy to dissect sphingolipid regulatory networks that might be responsible for ceramide regulation and localization in senescence. We found that while both apoptotic and senescent cells exhibit elevated ceramide levels, only senescent cells display a marked depletion of sphingomyelins, especially very-long-chain species. Despite transcriptional upregulation of sphingomyelin synthase 1, enzymatic activity remained unchanged, suggesting impaired ceramide transport. Pharmacological inhibition of Ceramide Transfer Protein (CERT), the ER-to-Golgi ceramide transporter, phenocopied the senescent sphingolipid profile and enhanced senescence markers. Furthermore, Raman spectroscopy revealed ceramide accumulation at the ER—but not the mitochondria—in senescent cells, consistent with a non-apoptotic phenotype. Together, our results identify disrupted ceramide turnover to sphingomyelin as a key feature of senescence and highlight the importance of subcellular ceramide localization in determining cell fate.

INTRODUCTION

Ceramides are central molecules in sphingolipid metabolism and are synthesized de novo through a highly regulated enzymatic pathway[1, 2]. The process begins at the endoplasmic reticulum (ER) membrane with the condensation of serine and palmitoyl-CoA, catalyzed by serine palmitoyltransferase (SPT), producing 3-ketosphinganine (**Scheme 1A**). This intermediate is reduced to sphinganine and subsequently N-acylated by ceramide synthases (CerS), which attach specific fatty acyl chains to generate dihydroceramides. These dihydroceramides are then desaturated by dihydroceramide desaturase (DES) to form ceramides. In addition to de novo synthesis, ceramides can also be generated via the hydrolysis of sphingomyelin by sphingomyelinases (SMases) or through the salvage pathway, where sphingosine, derived from the breakdown of complex sphingolipids, is re-acylated by CerS. Once formed, ceramides serve as precursors for complex sphingolipids, including glycosphingolipids and sphingomyelins, or can be metabolized into bioactive lipids like sphingosine and sphingosine-1-phosphate. Their synthesis and turnover are tightly controlled within distinct subcellular compartments, such as the ER, Golgi apparatus, and mitochondria, ensuring their availability and functional specificity in diverse cellular processes (reviewed in[2])

Ceramides have attracted significant attention as they are involved in diverse cellular processes, including apoptosis, senescence, autophagy, and endoplasmic reticulum stress[3-6]. The mechanisms and consequences of ceramide accumulation have been most extensively studied in the context of apoptosis. Elevated ceramide levels at the mitochondria have been shown to disrupt mitochondrial integrity, permeability, and function, thereby promoting cell death[7]. Notably, ceramide production localized to the mitochondria induces apoptosis, emphasizing that the cellular localization of ceramides can be linked to their distinct roles in various cellular processes[8]. Mechanistically, ceramides promote apoptosis by forming ceramide channels in the outer mitochondrial membrane, which facilitate the release of cytochrome c and other pro-apoptotic factors[7,9]. They also disrupt mitochondrial membrane integrity by interacting with key regulatory enzymes of the Bcl-2 protein family[10]. For example, ceramides inhibit phosphoinositide-3-kinase (PI3K) and Akt/PKB signaling, leading to the dephosphorylation and activation of pro-apoptotic proteins such as Bad[11]. Furthermore, ceramides can facilitate the translocation and oligomerization of BAX at the mitochondria, compromising membrane integrity, and interacting with voltage-dependent anion channels (VDAC1 and VDAC2), amplifying apoptotic signaling[12]. These studies collectively underscore the critical role of mitochondrial ceramide accumulation in mediating specific interactions at the mitochondria that ultimately drive apoptosis (reviewed in[2]).

In addition to apoptosis, ceramides accumulate in replicative senescence—a state of irreversible cell cycle arrest characterized. Senescence is driven by stress-induced pathways, including the p53-p21

and p16-RB pathways, which inhibit cyclin-dependent kinases, preventing cell cycle progression. Several studies have reported ceramide accumulation during replicative[13, 14] and other senescence programming[15, 16], implicating these lipids in aging and age-related diseases [17]. Specifically, our previous studies demonstrated that genes involved in sphingolipid metabolism are enriched among transcripts that are differentially expressed during senescence[13, 14]. Other studies also showed that ceramides accumulate with aging[18], can induce senescence[18, 19], and inhibition of *de novo* ceramide biosynthesis reduced senescence.[20] Venable et al. reported a positive correlation between the population doubling (PD) and ceramide levels where ceramides accumulated up to 4-fold in senescent cells.[4] Overall, these studies suggest the critical roles of ceramides in senescence. However, the precise mechanisms by which ceramides and sphingolipids are reregulated in senescence remain poorly understood.

In this study, we investigate the regulation of ceramides and other sphingolipids during replicative senescence compared to apoptosis (**Scheme 1B**). Through comparative lipid profiling and gene expression analysis, we identify distinct sphingolipid regulatory patterns and candidate enzymes that modulate ceramide levels in senescence. The lipidomic analysis revealed that ceramides accumulate in both apoptosis and senescence, whereas sphingomyelins are significantly depleted only in senescence. Gene expression data indicated an upregulation of Golgi-localized, sphingomyelin synthase 1 (SMS1); however, enzymatic assays showed no significant change in its activity. To investigate the regulation of sphingomyelin levels, we inhibited ceramide transport from the ER to the Golgi via CERT, a key step in sphingomyelin synthesis. This inhibition led to a substantial depletion of sphingomyelins and an enhanced senescence phenotype. Additionally, Raman spectroscopy demonstrated that ceramide accumulates in the ER during senescence. Collectively, our findings suggest that ceramide transport from the ER is affected during senescence, leading to sphingomyelin depletion, and highlight the ER as a key site of ceramide accumulation in senescent cells.

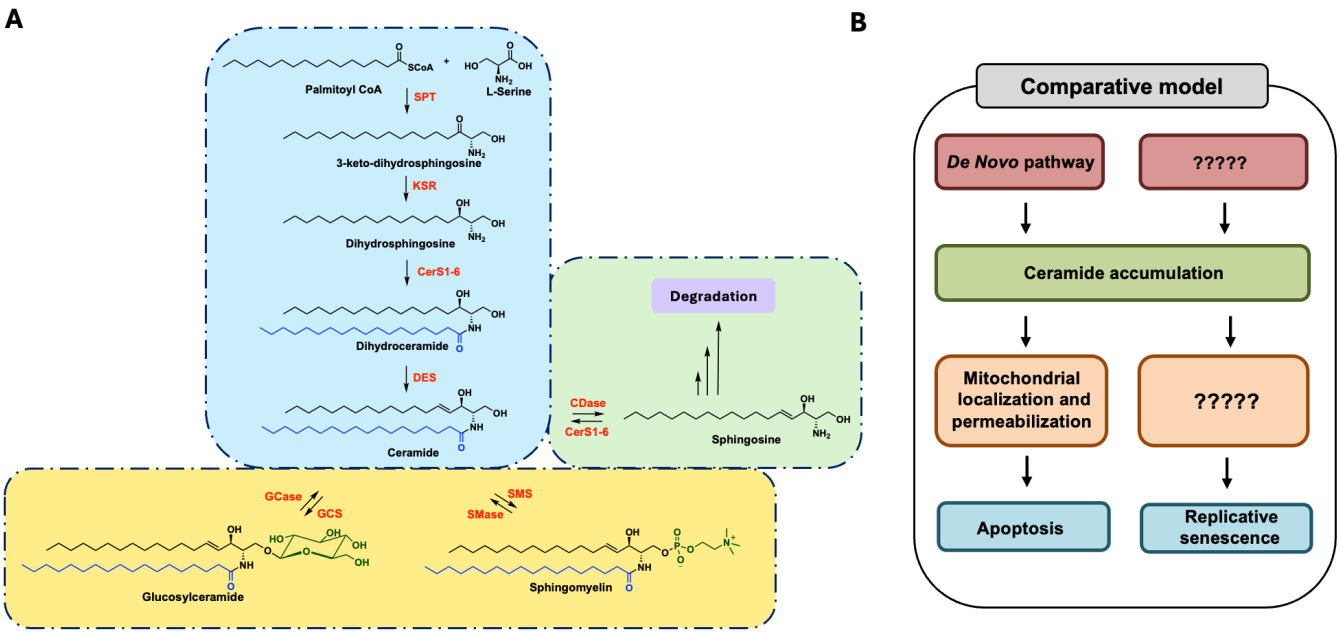

Scheme 1. (A) Sphingolipid biosynthesis pathway. Brief representation of sphingolipid biosynthesis. C18 fatty acyl chain containing sphingolipids are shown as representative structures. The enzymes involved in each step are indicated in red. The de novo ceramide synthesis pathway is highlighted in blue. Ceramides synthesized via this pathway can give rise to sphingomyelin and glucosylceramide (shown in yellow), or undergo further metabolism to sphingosine (shown in green). SPT: serine palmitoyl transferase; KSR: 3-keto-dihydrosphingosine reductase; CerS: ceramide synthase; DES: desaturase; SMS: sphingomyelin synthase; SMase: sphingomyelinase; GCS: glucosylceramide synthase; GCase: glucosylceramidase; CDase: ceramidase. **(B) Comparative model between senescence and apoptosis.** During apoptosis, ceramides generated via the de novo synthesis pathway are translocated to the mitochondria, where they accumulate and ultimately trigger cell death through apoptotic mechanisms. In contrast, ceramide accumulation also occurs during replicative senescence; however, the specific source and subcellular localization of ceramides remain unclear.

RESULTS AND DISCUSSIONS

Comparative analysis of replicative senescence with apoptosis. To investigate the regulation of ceramides in replicative senescence, we employed a comparative experimental framework that integrates both senescence and apoptosis as model systems. In this context, apoptosis serves as a

robust reference point for identifying senescence-specific regulatory mechanisms since ceramide dynamics are well-characterized in this process. By leveraging this comparison, we aimed to uncover sphingolipid species and regulatory enzymes that are differentially modulated in senescent cells. We combined lipidomics and gene expression analyses, enabling a comprehensive investigation of sphingolipid profiles and their associated gene expression changes. We envisioned that this framework provides a powerful platform to dissect how ceramide synthesis and metabolism diverges between apoptosis and senescence, ultimately offering insight into the distinct roles of ceramides in cellular aging and stress responses.

To carry out this comparative analysis, we used the human lung fibroblast cell line MRC-5, a well-established model for replicative senescence due to its well-established growth kinetics and senescence-associated phenotypes[13, 14]. MRC-5 cells typically undergo approximately 70 population doublings (PD) before entering senescent state. In our experiments, cells at early population doublings (~PD 14) were designated as "young," while cells at ~PD 60 were considered "senescent" based on hallmark characteristics such as increased senescence-associated β-galactosidase (SA-β-gal) activity and cessation of proliferation.[14] We observed a linear proliferation phase up to ~PD 35–40, after which the growth rate declined significantly, consistent with previous reports (**Figure S1A** and ref[13, 14]).

Cell pellets from both young/proliferating and old/senescent populations were harvested and stored for downstream lipidomic and transcriptomic profiling, following established protocols[21]. To establish a comparable apoptotic model, we treated young MRC-5 cells with doxorubicin (Dox), a DNA-damaging agent known to induce apoptosis and modulate sphingolipid metabolism. Based on dose-response viability assays, 2 μM Dox, which yielded ~60% cell viability, was selected for further experiments (**Figure S1B**). This dual-model system, replicative senescence and apoptosis, enables a direct comparison of ceramide and broader sphingolipid dynamics, along with gene expression changes, across two physiologically distinct cellular states. We envisioned that this framework sets the foundation for uncovering functional distinctions in sphingolipid metabolism during senescence and programmed cell death.

Sphingolipid Profiling Reveals Divergent Regulatory Patterns in Senescence and Apoptosis. To investigate sphingolipid dynamics in both apoptosis and replicative senescence, we analyzed lipid profiles from senescent and apoptotic MRC-5 cells compared to their respective control groups. Lipids were extracted using previously established protocols.[15, 16] Extracts were normalized to total protein content and reconstituted in chloroform. Comprehensive sphingolipid profiling was performed using liquid chromatography coupled to quadrupole time-of-flight mass spectrometry (LC-QTOF-MS).

The targeted analysis included several major sphingolipid classes: ceramides, dihydroceramides, hexosylceramides, sphingomyelins, and dihydrosphingomyelins. We first examined total levels of each class in senescent and apoptotic cells (**Figure 1A–B**). Ceramides were significantly elevated in both conditions, with hexosylceramides following a similar trend. Interestingly, sphingomyelins exhibited opposite patterns, showing marked depletion in senescent cells, while significantly increasing in apoptotic cells.

To gain finer resolution, we next assessed individual sphingolipid species. Heatmaps showing relative abundances (**Figure 1C–D**) revealed distinct regulatory trends. In senescent cells, most ceramide and hexosylceramide species were significantly enriched, particularly those with long-chain (C16–C18) and very-long-chain (C20–C24) acyl groups. In contrast, nearly all sphingomyelin species were depleted. Apoptotic cells showed elevation of ceramides and sphingomyelins, but only a subset of hexosylceramides (C18:1 and C18:0) were increased.

The divergent sphingomyelin trends are particularly striking. In senescence, the consistent depletion of sphingomyelins suggests altered enzymatic activity in ceramide metabolism. This may reflect either downregulation of sphingomyelin synthase activity or enhanced sphingomyelin degradation through activation of sphingomyelinases, which would yield additional ceramide and reinforce its accumulation. Given the preferential enrichment of very-long-chain ceramides in senescence, this shift may also reflect increased turnover of very long chain sphingomyelin species.[22] Overall, these results suggest that ceramide turnover may differ between senescence and apoptosis.

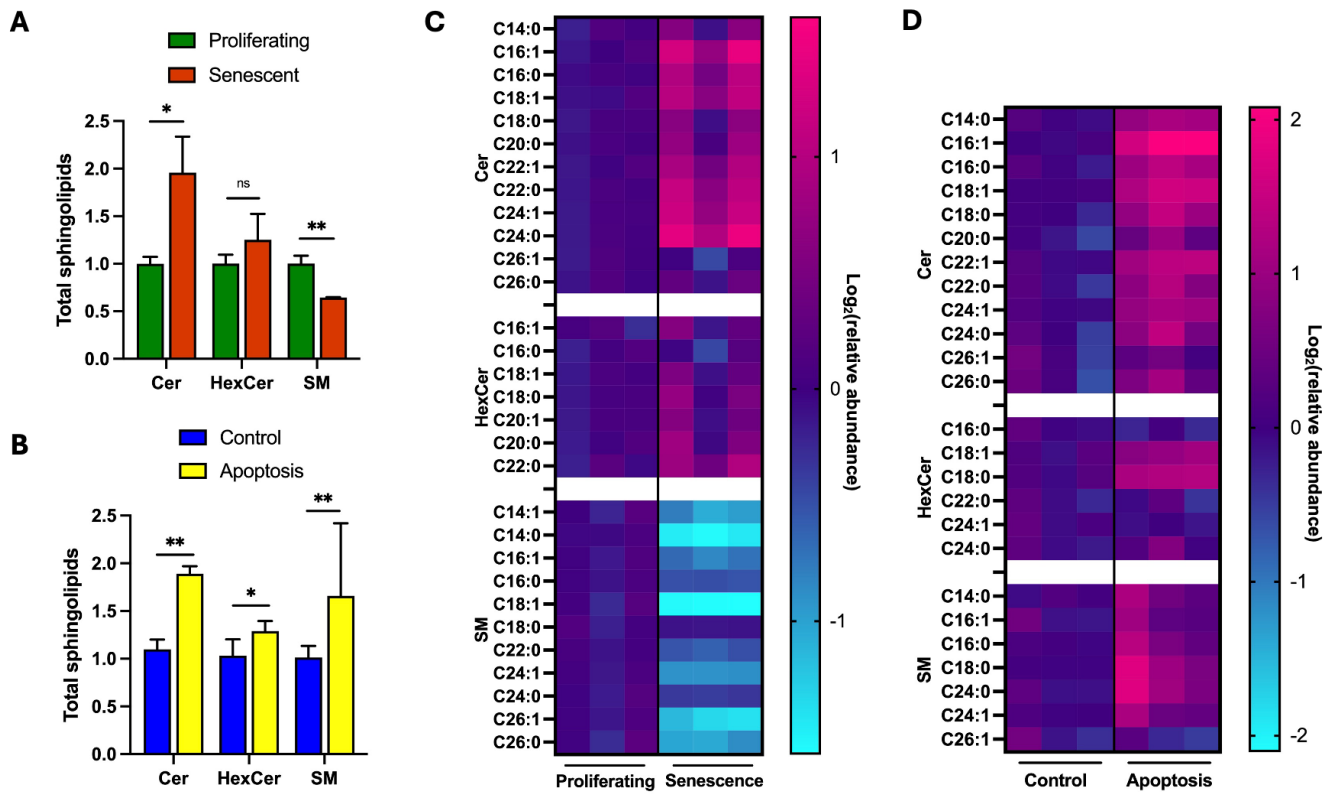

Figure 1. (A-B) Total sphingolipids level for proliferating and senescent vs control and apoptosis in MRC5 cells (n=3 for each condition). **(C-D)** Heatmaps representing sphingolipid levels in senescence and apoptosis model. Pink represents accumulation, and blue represents depletion. The relative abundances are reported as $\log_2$(relative abundances). N=3 for each condition. * represents $p<0.05$, ** represents $p<0.01$, ns represents not significant. Cer: ceramide; HexCer:hexosylceramide; SM: sphingomyelin.

Gene Expression Analysis Reveals Differential Regulation of Sphingolipid Biosynthetic Enzymes in Senescence and Apoptosis. Lipidomic profiling revealed distinct sphingolipid signatures in senescence and apoptosis: ceramides were elevated in both models, but sphingomyelins showed differential regulation, significantly depleted in senescent cells while elevated in apoptotic cells. To better understand the regulation of these trends, we examined the expression of key genes involved in sphingolipid metabolism. Total RNA was extracted from MRC-5 cells representing each model (proliferating and senescent cells for the senescence model, untreated and doxorubicin-treated cells for the apoptosis model), and gene expression was quantified. We measured the expression of genes regulating de novo ceramide synthesis, catabolism, and downstream metabolic branching (**Figure S2**).

We then focused on genes that show differential regulation in senescence as compared to the apoptosis model. The changes in expression trend of these genes is listed in **Figure 2A**. In senescent cells, several key enzymes were significantly upregulated: SPT (serine palmitoyltransferase, ER-

localized) and DEGS1 (dihydroceramide desaturase, ER-localized), which drive de novo ceramide biosynthesis; A-CDase and A-SMase (lysosome-localized acid ceramidase and sphingomyelinase, respectively), which regulate ceramide turnover; and SMS1 (sphingomyelin synthase 1) and GCS (glucosylceramide synthase), both localized to the Golgi and responsible for ceramide conversion into downstream sphingolipids (**Figure 2A**). This transcriptional signature suggests an upregulation of both ceramide production and potential utilization pathways during senescence. In contrast, apoptotic cells exhibited a distinct expression profile. While A-SMase was upregulated, genes such as SPT, DEGS1, A-CDase, and SMS1 showed no significant change, and GCS was downregulated compared to controls (**Figure 2A**).

Importantly, when integrating gene expression data with lipidomic findings, a key observation emerges: SMS1, the enzyme responsible for ceramide-to-sphingomyelin conversion, is upregulated in senescent cells (**Figure 2A-B**), yet sphingomyelin levels are markedly depleted (**Figure 1**). This disconnect suggests that despite increased transcription of SMS1, ceramide conversion to sphingomyelin may be functionally impaired during senescence. At the functional level, SMS exhibits similar activity between senescent and proliferating cells (**Figure 2C**), supporting the idea that the decreased SM levels may be due to impaired transport of ceramides from ER to Golgi. These observations raise the intriguing possibility that the regulation of ceramide-to-sphingomyelin flux, rather than ceramide synthesis per se, may be an important contributor to ceramide's senescence-specific activity.

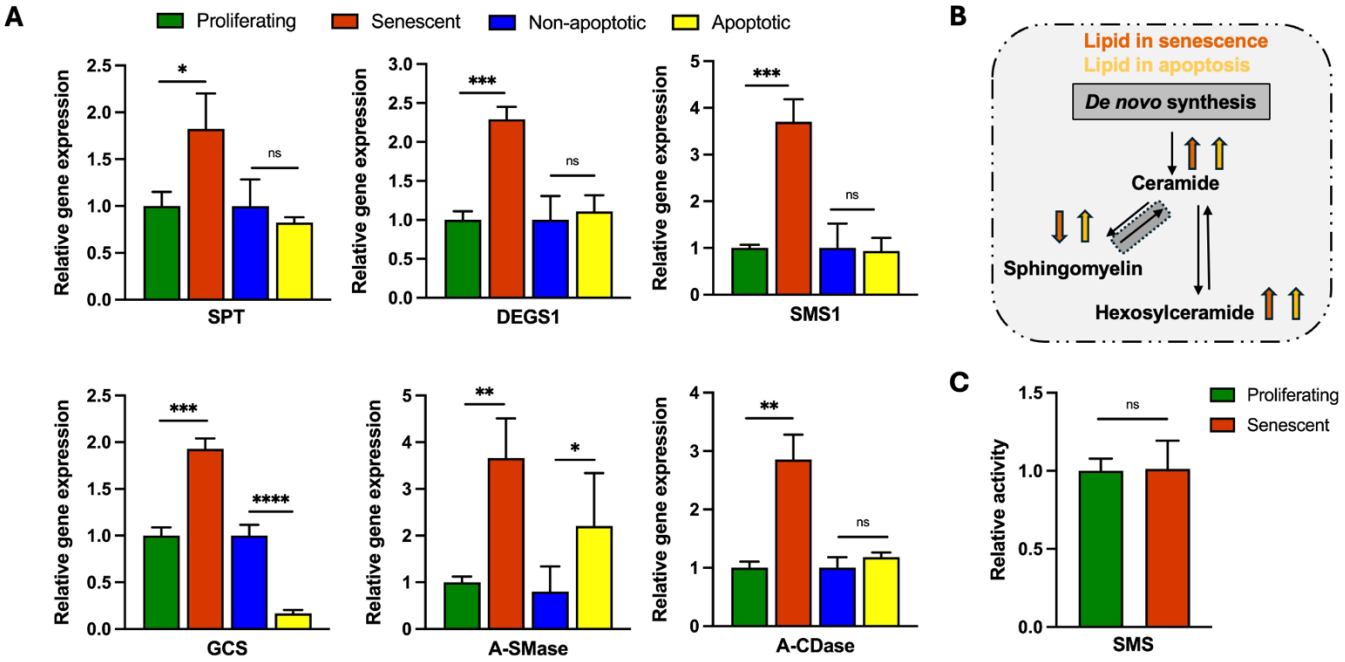

Figure 2. Differential regulation of sphingolipid-related genes and lipid profiles in senescence and apoptosis. (A) Relative gene expression levels of sphingolipid-metabolizing enzymes in senescent and apoptotic MRC-5 cells. Gene expression was normalized to the housekeeping gene HPRT1. Data represent n = 3 biological replicates for senescent cells and n = 5 for apoptotic cells. $p < 0.05$ (*), $p < 0.01$ (**), $p < 0.001$ (***), $p < 0.0001$ (****); ns = not significant. **(B)** Schematic summary of key lipid changes observed in senescence and apoptosis based on lipidomic profiling. (**C**) SMS1 remain the same in senescent cells compared to proliferating one. The amount of C6-Sphinogmyelin produced from C6-Ceramide was measured using LC-QToF-MS.

Blocking Ceramide Transport from ER to Golgi Exacerbates Senescence. We observed a marked depletion of sphingomyelins, particularly very-long-chain species, while no appreciable changes were observed at the enzymatic level during senescence. This suggests that additional factors beyond enzyme expression, such as ceramide transport, may be affecting sphingomyelin synthesis. Notably, the non-vesicular transfer of ceramides from the ER to the Golgi is mediated by CERT, which plays a critical role in ceramide trafficking[23]. Based on these observations, we decided to target ceramide transport to the Golgi and hypothesized that a functional bottleneck at the level of CERT-mediated transport could contribute to the observed accumulation of ceramides and depletion of sphingomyelins in senescent cells.

To test this, we targeted CERT using HPA12, which disrupts ceramide transport from the ER to the Golgi (**Figure 3A**)[24]. We reasoned that blocking this transport step should exacerbate ceramide retention at the ER and phenocopy the sphingolipid changes observed in senescence. Dose-response studies identified 3 μM and 10 μM HPA12 as concentrations with minimal impact on cell viability (**Figure S3A**). Treatment of young MRC-5 cells with HPA12 led to a significant, dose-dependent increase in SA-β-galactosidase-positive cells, with 1.75-fold and 2.75-fold increases observed at 3 μM and 10 μM, respectively (**Figure 3B**), indicating increased senescence levels.

To assess the impact of CERT inhibition on sphingolipid composition, we performed lipidomic analysis on HPA12-treated cells. While total ceramide levels remained unchanged (**Figure 3C**), there was a clear depletion of sphingomyelins, particularly those containing very-long-chain fatty acids (5-10-fold, $p < 0.05$), consistent with impaired ceramide utilization in the Golgi (**Figure 3D**). This observation supports our earlier gene expression data suggesting that while the enzymatic machinery for sphingomyelin synthesis is unaffected, the transport of ceramides to the Golgi may be limiting in senescence. These findings support a model in which disrupted ceramide transport via CERT inhibition recapitulates key features of senescence, including sphingolipid imbalance and increased senescence-

associated activity. They also underscore the importance of spatial control in ceramide metabolism, highlighting CERT as a critical regulator of lipid remodeling during this process.

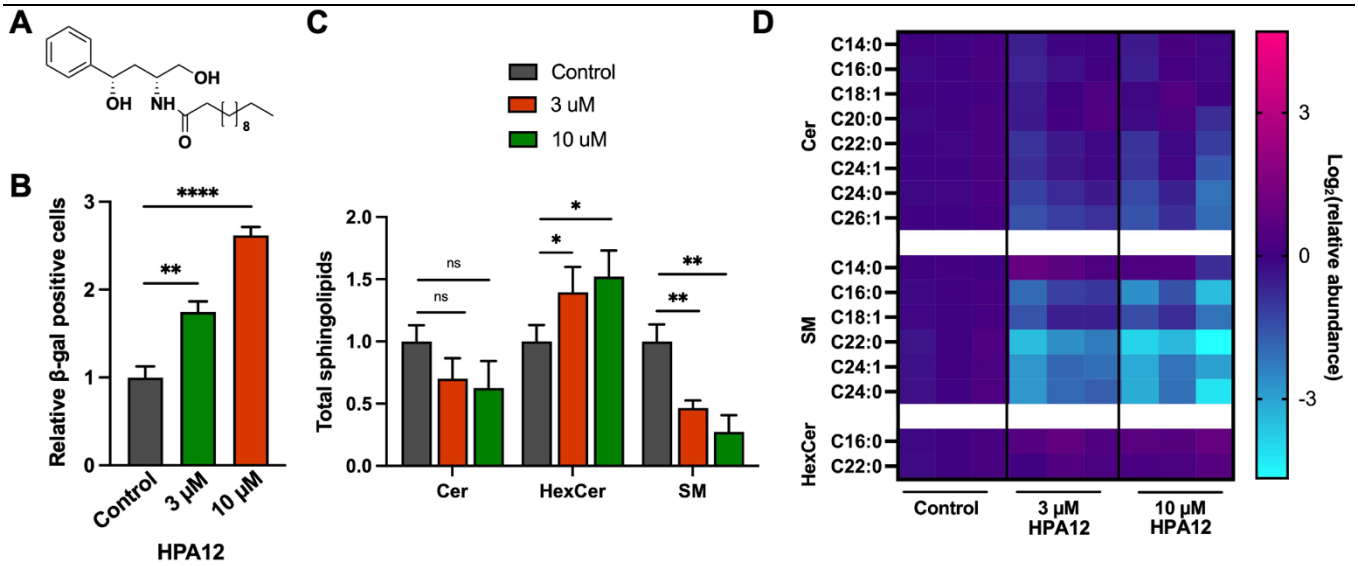

Figure 3. Inhibition of CERT-mediated ceramide transport and SMS enhances senescence and alters sphingolipid profiles in MRC-5 cells. (A) Structure of the CERT inhibitor, HPA12. **(B)** Senescence-associated β-galactosidase (SA-β-gal) assay showed an increase in senescence in MRC-5 cells treated with 3 μM and 10 μM HPA12 compared to untreated controls. **(C)** Total sphingolipid levels in MRC-5 cells following treatment with 3 μM and 10 μM HPA12, as measured by LC-QTOF-MS. **(D)** Heatmaps displaying relative abundances of individual sphingolipid species in MRC-5 cells treated with 3 μM and 10 μM HPA12. Data represent n = 3 biological replicates for senescent cells and n = 5 for apoptotic cells. $p < 0.05$ (*), $p < 0.01$ (**), $p < 0.001$ (***), $p < 0.0001$ (****); ns = not significant.

Raman-BCA suggests increased ceramide localization at the ER during senescence. To gain insight into ceramide trafficking and localization during senescence, we integrated traditional fluorescence microscopy and quantitative Raman Spectrometry coupled to the Biomolecular Component Analysis Algorithm (Raman BCA or Ramanomics)[25] to monitor ceramide localization in senescent cells. Raman BCA selectively recognizes many types of biomolecules and enables studies of the molecular composition in single organelles[26, 27]. Further, in contrast to largely qualitative or semi-quantitative fluorescence measurements, the Raman-BCA approach can quantitatively determine the molecular concentrations at the site of spectra measurements in live cells.

Alkynyl probes are highly effective for Raman sensing in live cells due to their unique spectroscopic properties and biorthogonality. The carbon-carbon triple bond (-C≡C-) produces a distinct Raman signal in the cellular silent region (1800–2800 cm^{-1}), minimizing spectral overlap with endogenous

biomolecules and enabling high-contrast imaging. The small size of -C≡C- allows for minimal perturbation of cellular function, making them ideal for live-cell applications. The chemical versatility facilitates conjugation to a wide range of biomolecules, including proteins, lipids, and nucleic acids, allowing for targeted imaging of specific cellular structures and processes. Furthermore, unlike conventional fluorescent probes, alkynyl probes demonstrate high stability, reducing signal loss over extended imaging periods. These properties make alkynyl probes a powerful tool for studying dynamic cellular events with high specificity and minimal interference.[28]

We took advantage of the biorthogonal nature of the alkynyl group in generating the Raman signal in live cells and used C6-alkynyl ceramide and first established that alkynyl ceramide exhibits a distinctive Raman peak at ~2100 cm^{-1}.[27] We then used this peak to map the localization of ceramides in proliferating vs. senescent cells in different organelles, relevant for ceramide metabolism. We utilized LysoTracker Green DND-26, ER-Tracker Green and Mito-tracker Green to fluorescently label lysosomes, ER, and mitochondria in live cells.[29] Data acquisition and analysis are carried out as described previously.[27] Briefly, Raman spectra were collected from the fluorescently-labeled organelles in live proliferating and senescent cells and used to calculate the ceramide concentrations based on the peak intensity around ~2100 cm^{-1} (**Figure 4A**). We found that C6-alkynyl ceramide was significantly accumulated at the ER in senescent cells compared to proliferating cells while levels at the mitochondria were reduced and lysosomal levels remained the same (**Figure 4B**). Collectively, these findings provide strong support for our hypothesis that ceramides accumulate at the ER during cellular senescence.

Ceramide-Induced ER Stress as a Mechanistic Driver of Cellular Senescence. Ceramides can accumulate in the ER under metabolic and oxidative stress conditions.[30, 31] This accumulation can perturb ER membrane composition and impair protein folding capacity, thereby initiating ER stress and activating the unfolded protein response (UPR).[32] Persistent ER stress has been closely associated with the onset of cellular senescence. Increasing evidence suggests a bidirectional relationship between ER stress and senescence, whereby ER stress not only arises as a consequence of senescence but also serves as a causal factor in its initiation and maintenance.[33] Central mediators of the UPR, such as protein kinase RNA-like endoplasmic reticulum kinase (PERK) and activating transcription factor 6 (ATF6), have been shown to modulate senescence-associated gene expression.[34, 35]

Emerging evidence suggests that ceramide-mediated ER stress may serve as a mechanistic link between lipid metabolism dysregulation and the establishment of senescence [36]. To determine whether ceramide accumulation at the ER contributes to ER stress during senescence, we first assessed the expression levels of key ER stress markers, including C/EBP homologous protein (CHOP) and activating transcription factor 6 (ATF6). Both markers exhibited increased expression in senescent cells compared

to proliferating cells (**Figure 4C**), supporting increased ER stress during senescence. We then conducted a co-treatment experiment of HPA12 with thapsigargin to block the ER to Golgi transport of ceramide and induce ER stress, respectively [37] and measured the senescence levels using SA-β-gal assay (**Figure 4D**). Exposure to the ER stressor thapsigargin (0.03 μM) leads to a ~3-fold increase in SA-β-gal-positive cells compared to controls, indicating that even mild disruption of ER calcium homeostasis is sufficient to elicit a robust senescence response. Consistent with our previous findings, pharmacological inhibition of CERT using HPA-12 (3 μM) yields a comparable increase in senescent cells, suggesting that impaired ceramide trafficking and disrupted sphingolipid balance independently trigger senescence to a similar extent. Notably, co-treatment with thapsigargin and HPA-12 results in a ~6-fold elevation in SA-β-gal positivity, surpassing the effect of either agent alone and pointing to at least an additive interaction. Mechanistically, the combined effects of ER stress and ceramide accumulation within the ER may synergistically enhance unfolded protein response signaling and cellular stress, thereby increasing the proportion of cells undergoing irreversible growth arrest. Together, these findings demonstrate that both ER stress and lipid homeostatic disruption independently promote senescence, and their convergence amplifies the senescent phenotype, underscoring the interplay between ER stress and ceramide accumulation at the ER in senescence regulation. Based on these and other findings suggesting ceramide accumulation at the ER, we propose that ER-localized ceramide accumulation may drive ER stress, thereby contributing to the induction of cellular senescence.

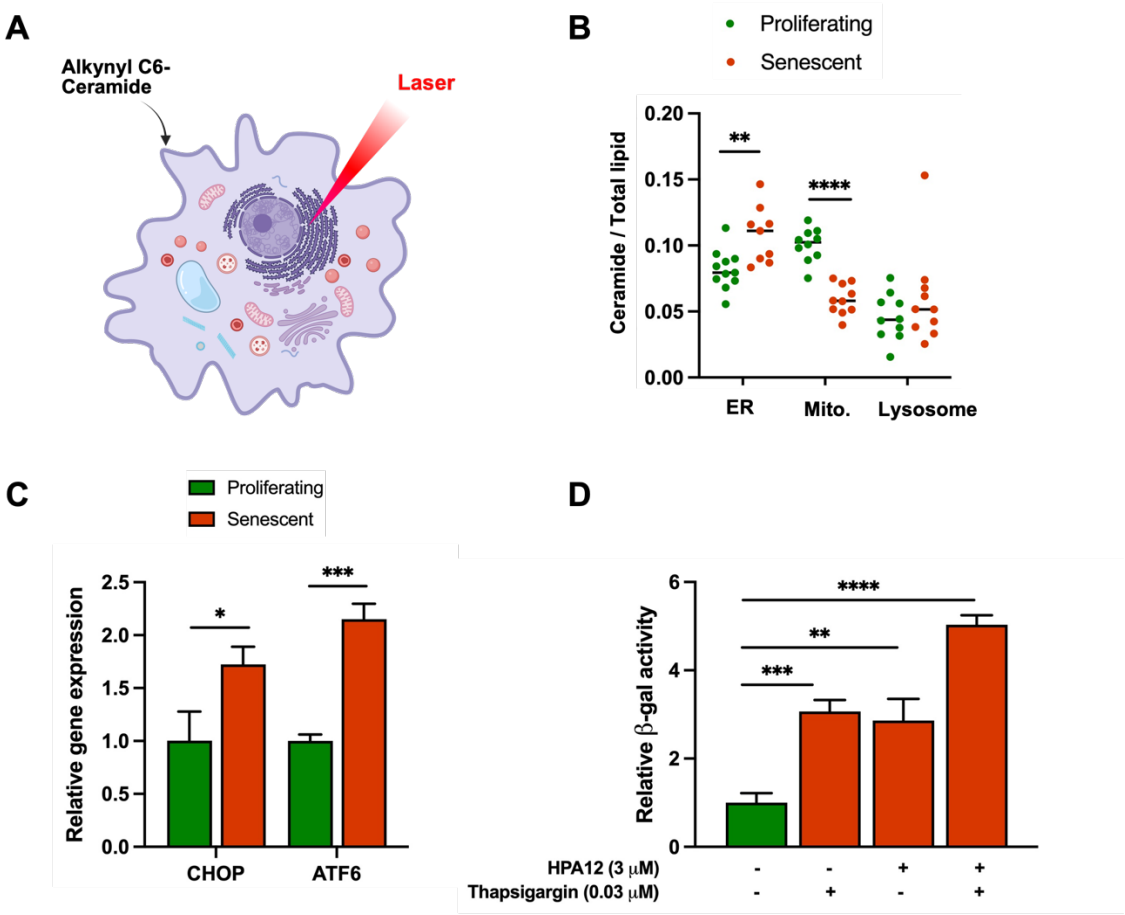

Figure 4. (A) Schematic representation of Raman-BCA to understand the localization of ceramide in senescence. **(B)** Raman measurements for young and senescent cells pre-incubated with C6-ceramide alkyne probe, followed by imaging of the organelles: endoplasmic reticulum, mitochondria, and lysosome. **(C)** Relative gene expression levels for the ER stress markers: CHOP (C/EBP homologous protein), ATF6 (activating transcription factor 6). **(D)** Senescence-associated β-galactosidase (SA-β-gal) assay for co-treatment of HPA12 (3 μM) and thapsigargin (0.03 μM) compared to individual treatments and untreated controls.

CONCLUSIONS

Ceramides are bioactive sphingolipids known to regulate diverse cellular processes, including apoptosis and senescence. While it has been established that ceramides accumulate during the senescence, the regulatory mechanisms and subcellular localization of ceramides in this process remain incompletely understood. In this study, we investigated how ceramides are distinctly regulated in replicative senescence using a comparative model of apoptosis and senescence. Through integrated lipidomic and transcriptomic profiling, we observed that while both senescent and apoptotic cells exhibited elevated ceramide and hexosylceramide levels, sphingomyelins were significantly depleted in

senescent cells but increased during apoptosis. Notably, in senescent cells, very-long-chain sphingomyelin species were most strongly reduced, prompting us to focus on the role of SMS in regulating ceramide flux. Despite increased transcription of SMS1, enzymatic activity remained unchanged, suggesting that it is not the SMS activity that causes reduced sphingomyelin levels. We hypothesized that impaired ER-to-Golgi transport can mediate the changes in ceramide and sphingomyelin dynamics we observe in senescence.

To test this hypothesis, we disrupted ceramide trafficking by inhibiting CERT, the ER-to-Golgi ceramide transfer protein. CERT inhibition recapitulated the sphingolipid imbalance seen in senescent cells and significantly enhanced senescence markers in proliferating cells. Similarly, pharmacological inhibition of SMS further promoted ceramide accumulation and senescence, supporting a model in which impaired ceramide metabolism drives senescence-associated phenotypes. Using quantitative Raman-BCA, we also demonstrated that ceramides accumulate at the ER in senescent cells. Importantly, mitochondrial ceramide accumulation—characteristic of apoptotic signaling—was not observed, consistent with a non-apoptotic, pro-senescent role for ceramide in this context.

Ceramide accumulation at the ER has been shown to initiate ER stress responses in various models, primarily through activation of the unfolded protein response and downstream effectors.[38, 39] Concurrently, ER stress has emerged as a potent inducer of cellular senescence, contributing to the activation of key pathways involved in growth arrest.[40] Despite these parallel observations, a direct mechanistic connection linking ceramide accumulation at the ER to senescence has remained unclear. Our findings help bridge this gap by demonstrating that ceramides accumulate at the ER during replicative senescence, rather than at the mitochondria where they typically promote apoptosis. This ER-localized accumulation coincides with impaired ceramide flux to the Golgi, as evidenced by sphingomyelin depletion and preserved SMS1 activity despite increased expression. Together, these data suggest that ceramides are retained within the ER, where they may act as endogenous stressors that contribute to ER dysfunction and the establishment or maintenance of the senescent phenotype. Thus, our work proposes a framework in which ER-localized ceramide accumulation serves as a molecular trigger for ER stress–driven senescence. Together, these findings highlight the importance of ceramide compartmentalization and transport in regulating cell fate and identifies ceramide turnover through SMS as a critical metabolic control point during cellular senescence.

SUPPLEMENTAL INFORMATION

Supplemental information includes 3 figures and 4 tables.

ACKNOWLEDGMENTS

We acknowledge the support from the National Science Foundation grant (MCB 2314338 to G.E.A.G.). We would like to thank Karla I Garcia-Gonzalez for her assistance in generating lipidomics data.

AUTHOR CONTRIBUTIONS

Experiments were designed by S.C. and G.E.A-G. The experiments were conducted by S.C., N.G., A. P., and A. K.. S.C, N. G., conducted the lipidomics, gene expression analysis and other biochemical assays. A.P., A. K. and P.P. designed and supervised Raman experiments. Y.S. provided critical feedback in data interpretation and manuscript preparation. The manuscript was written by S.C. and G.E.A-G. The study was directed by G.E.A-G.

The authors declare no conflict of interest.

MATERIALS and METHODS

Materials

MRC-5 cell line (human lung fibroblasts) was purchased from the American Type Culture Collection. Eagle's Minimum Essential Medium (EMEM), penicillin-streptomycin, and trypsin were sourced from Corning. Fetal Bovine Serum (FBS) and doxorubicin were acquired from Millipore Sigma. Dimethyl sulfoxide (DMSO) was obtained from Acros Chemicals. Senescence-associated β-galactosidase staining kit was obtained from Cell Signaling. LC-MS columns and guard cartridges were purchased from Phenomenex. Lipid standards were obtained from Avanti Polar Lipids and Cayman Chemical. All solvents were LC-MS grade and purchased from Millipore Sigma. iScript Advanced cDNA conversion kit was purchased from Bio-rad. E.Z.N.A Total RNA kit 1 was purchased from Omega Biotek. MTT reagent was purchased from Sigma. The senescence β-galactosidase staining kit was sourced from Cell Signaling. HPA12 and D609 were purchased from Cayman Chemicals. Chloroquine and puromycin were purchased from Sigma. ER-Tracker™ Green (BODIPY™ FL Glibenclamide), LysoTracker™ Green DND-26 and MitoTracker™ Green FM Dye were bought from Invitrogen.

Methods

Cell Culture for senescence. MRC-5 cells, obtained at a population doubling (PD) ~ 14 were cultured in EMEM supplemented with 10% FBS and 1% penicillin-streptomycin. Cells were grown in a humidified incubator at 37 °C and 5% CO_2. To achieve senescence, the cells were cultured to about PD ~ 69 (referred to as old/senescent cells hereon) in 10 cm cell culture dishes. Cell pellets were collected at population doublings 24 (young) and 69 (old).

Doxorubicin-induced apoptosis. 1 x 10^6 MRC-5 cells were plated in a 10 cm cell culture dishes and incubated for 16 hours. After 16 hours, the cells were treated with Doxorubicin (Dox) such that the final concentration of Dox in the plate is 2 μM and the control plates were treated with an equal volume of DMSO followed by incubation for 24 hours before collecting cell pellets. Cells were collected by removing cell media in a 15 mL falcon, washing with 2.5 mL cold 1XPBS twice, and then scraping. The cell suspension was centrifuged (300 rcf, 5 min, 4 °C). PBS was removed, and the cell pellet was gently resuspended in cold 1XPBS to remove any residual media and centrifuged again (300 rcf, 5 min, 4 °C). Cell pellets were stored at -80 °C until lipid extraction was performed.

Lipid extraction. Lipid extraction was performed using previously reported protocols [15]. Briefly, cell pellets were resuspended in 1 mL cold 1X PBS, 50 μL of which was set aside to be used for measuring protein concentration using the Coomassie (Bradford) Protein Assay Kit as per the protocol provided by the manufacturer. The remaining cell suspension in PBS was then transferred to a homogenizer to which 2 mL of chloroform and 1 mL of methanol was added. The solution was homogenized 30 times using a glass Dounce tissue grinder. The homogenized solution was centrifuged at 500 rcf, 4°C for 10 minutes to separate aqueous and organic layers. The organic layer was carefully removed and dried under a vacuum. Samples were then resuspended in chloroform spiked with internal standard based on total protein concentration.

LC-QTOF-MS Acquisition. Liquid Chromatography coupled to quadrupole time-of-flight mass spectrometry (LC-QTOF-MS) -based lipidomics analysis was performed using an Agilent 1260 high-performance liquid chromatography instrument paired with an Agilent 6530 jet stream electrospray ionization quadrupole time-of-flight mass spectrometer. Data was collected using an *m/z* range of 50-1700. For chromatographic separation, a Gemini C18 reversed-phase column (5μm, 4.6 mm x 50 mm, Phenomenex) with a C18 reversed-phase guard cartridge was used in negative electrospray mode, and a Luna C5 reversed-phase column (5 μm, 4.6 mm x 50 mm, Phenomenex) with a C5 reversed-phase guard cartridge was used in positive electrospray mode. Mobile phase A was constituted of 95:5 water:methanol (v/v) and mobile phase B was constituted of 60:35:5 isopropanol:methanol:water (v/v) in both negative and positive mode. For negative detection, 0.1% (v/v) ammonium hydroxide was added each mobile phase. For positive detection, 0.1% (v/v) formic acid and ammonium formate were added to mobile phases. The flow rate was set to 0.1 mL/min for the first 5 minutes followed by an increase to 0.5 mL/min for the remainder of the gradient. The gradient started at 5 minutes with 0% B to 100% B over 60 minutes. Starting at 65 minutes an isocratic gradient was applied at 100% B for 7 minutes. Equilibration

of the column followed with 0% B for 8 minutes. An electrospray ionization source was used with a capillary voltage of 3500 V and fragmenter voltage of 175 V.

Data Analysis for Targeted Lipidomics. For targeted lipidomics, three biological replicates of each condition in both models, young and senescent in the senescence model, control and dox-treated in the apoptosis model were used in positive and negative electron spray mode. Targeted data analysis was performed using the Agilent MassHunter Qualitative Analysis software by importing the raw data obtained from LC-QTOf-MS. The *m/z* for each ion was extracted and the peak area for each ion was manually integrated. Fold change was calculated as (Abundance $_{senescent}$) / (Abundance $_{Young}$) or (Abundance $_{Dox\text{-}treated}$) / (Abundance $_{Control}$) for each species.

RNA extraction and cDNA Conversion. Approximately 1 x 10^6 cells were collected for both models as described above. Total RNA was extracted for each condition using E.Z.N.A. Total RNA Kit I. The protocol provided by the manufacturer was followed. RNA concentration was measured using a Nanodrop-1000 spectrophotometer (Thermo). Three biological replicates were taken in each case. The extracted RNA was converted into its complementary DNA using reverse transcription using the iScript cDNA Synthesis kit following the manufacturer's instructions.

Droplet Digital Polymerase Chain Reaction (ddPCR). Reaction mixtures were prepared in a 96-well plate by combining the cDNA, ddPCR Supermix, primers, and probes according to Bio-Rad's protocol for the Droplet Digital PCR: QX200 System. BioRad Automated Droplet Generator was used to generate water-in-oil emulsion droplets and transferred to a new 96-well plate, which was heat-sealed using foil sheets. Target genes and reference gene, Hypoxanthine phosphoribosyltransferase 1 were amplified by thermal cycling the droplet emulsions as follows: 95 °C for 10 minutes (DNA polymerase activation), 40 cycles of 94 °C for 30 seconds (denaturation), 56 °C for 60 seconds (annealing and extension) with a final 10-minute inactivation step at 98 °C. The fluorescence of each thermally cycled droplet was measured using the QX200 droplet reader. Data was analyzed using Bio-Rad's QuantaSoft software after threshold setting on the fluorescence of negative controls. Refer to SI Table 3 for the list of primers used to measure mRNA expression.

Dose-response profile for small molecules. MTT assay was used to obtain a dose-response curve for HPA12. About 2 x 10^4 MRC-5 cells per well were plated in a 96-well plate and incubated for 16 hours. Cells were treated with varying concentrations of HPA12: 0 μM, 1 μM, 3 μM, 10 μM and 30 μM, followed by 72 hours of incubation. After 72 hours, the media containing the treatment was removed from the

wells, and 9% MTT solution in the media was added to the wells. The cells were incubated for 2-2.5 hours to allow the conversion of MTT to formazan crystals, which were later dissolved in DMSO. The absorbance was measured using a plate reader and was used to generate a dose-response curve.

Senescence-associated β-galactosidase assay for small molecules. Approximately 7 x 10^3 MRC-5 cells per well were seeded in 24-well. After 24 hours of seeding, cells were treated with 3 μM and 10 μM of HPA12 and incubated for 72 hours. Senescence-associated β-galactosidase activity was assessed after 72 hours of treatment using the Senescence β-galactosidase staining kit from Cell Signaling according to the manufacturer's instructions. After treatment, cells were washed once with pre-warmed 1X PBS and fixed using a fixation buffer for 10-15 minutes. The cells were then washed twice more with PBS and incubated for 20 hours at 37 °C in freshly prepared staining buffer containing X-gal (5-bromo-4-chloro-3-indolyl β-D-galactopyranoside). After 20 hours of incubation, cells were washed with 1xPBS and observed under a light microscope to determine the percentage of SA-β-galactosidase positive cells (n ≥ 200 cells per condition, n=3).

SMS enzymatic activity assay. The activity assay was adapted from previous protocols. Both proliferating and senescent cells were collected, followed by lysis using probe sonication (10s on, 10s off, for 3 times) in 200 μL buffer supplemented with EDTA-free protease inhibitor (Thermo Fischer) and phosphatase inhibitor cocktail 2 (Thermo Fischer). Neutral buffer (25 mM Tris, 12 mM $MgCl_2$, pH 7.5) containing EDTA-free protease inhibitor (one tablet per 10 mL) and phosphatase inhibitor cocktail 2 (100 μL of stock per 10 mL) was used for SMS enzyme assay. The assay was performed in triplicate in a 1.5 mL microcentrifuge tube, and each reaction mixture contained 80 μg of protein in 60 μL of buffer mixed with lipid standards (C6 ceramide and DOPC for SMS activity assay). Each reaction mixture was incubated at 37 ℃ for 3 hours. Then the reactions were quenched using methanol and were again incubated at 37 ℃ for 30 minutes. This was followed by samples being centrifuged, dried under vacuum, and resuspended in methanol. These samples were analyzed using LC-QTOF-MS for the production of C6-SM (in positive ionization mode; $[M+H]^+$, m/z= 563.4184).

Raman measurements and analysis. MRC5 cells were plated in glass glass-bottom petri dish and incubated overnight. The next day, the media (EMEM) was changed to phenol red-free media, Opti-MEM, followed by the addition of C6-ceramide alkyne probe (final concentration 25 μM) to both plates and incubated at 37 ℃ for 1 hour. After an hour, the organelle tracker was added to the plates and incubated for 20 minutes. Then the plates were washed with 1xPBS three times. Then Raman microscope DXR2

(Thermo-Fisher Scientific, Madison, WI), equipped with a laser source unit emitting ~60 mW at 633 nm (ROUSB-633-PLR-70-1, Ondax), a 50 μm pinhole to shape the laser beam to a 0.7×0.7×1.5 μm3 FWHM, a Plan N 100× Olympus objective lens (NA = 1.25) and fluorescence lamp (X-Cite 120 PC, Photonic Solutions), was used to measure Raman spectra of labelled organelles. Quantitative analysis of organellar spectra was performed using the *BCAbox* software (ACIS LLC, Buffalo, NY). Detailed description of the method, output (BCA) parameters and the calibration of Raman band intensities on the concentrations of biomolecules in the sample were described in our previous publications[27]. The alkyne has a significant intensity and wavenumber 2200 cm^{-1}. A total of 10-12 points were imaged and analyzed for the ratio of C6-ceramide alkyne to total lipid at each point. The organelles that were imaged for understanding the localization of ceramide during senescence were: endoplasmic reticulum, mitochondria and lysosome.

References

(1) Mullen, T. D.; Hannun, Y. A.; Obeid, L. M. Ceramide synthases at the centre of sphingolipid metabolism and biology. *Biochem J* **2012**, *441* (3), 789-802. DOI: 10.1042/BJ20111626 From NLM Medline.

(2) Chitkara, S.; Atilla-Gokcumen, G. E. Decoding ceramide function: how localization shapes cellular fate and how to study it. *Trends Biochem Sci* **2025**. DOI: 10.1016/j.tibs.2025.01.007 From NLM Publisher.

(3) Mullen, T. D.; Obeid, L. M. Ceramide and apoptosis: exploring the enigmatic connections between sphingolipid metabolism and programmed cell death. *Anticancer Agents Med Chem* **2012**, *12* (4), 340-363. DOI: 10.2174/187152012800228661 From NLM Medline.

(4) Venable, M. E.; Lee, J. Y.; Smyth, M. J.; Bielawska, A.; Obeid, L. M. Role of ceramide in cellular senescence. *J Biol Chem* **1995**, *270* (51), 30701-30708. DOI: 10.1074/jbc.270.51.30701 From NLM Medline.

(5) Pattingre, S.; Bauvy, C.; Levade, T.; Levine, B.; Codogno, P. Ceramide-induced autophagy: to junk or to protect cells? *Autophagy* **2009**, *5* (4), 558-560. DOI: 10.4161/auto.5.4.8390 From NLM Medline.

(6) Park, W. J.; Park, J. W. The role of sphingolipids in endoplasmic reticulum stress. *FEBS Lett* **2020**, *594* (22), 3632-3651. DOI: 10.1002/1873-3468.13863 From NLM Medline.

(7) Siskind, L. J.; Kolesnick, R. N.; Colombini, M. Ceramide channels increase the permeability of the mitochondrial outer membrane to small proteins. *J Biol Chem* **2002**, *277* (30), 26796-26803. DOI: 10.1074/jbc.M200754200 From NLM Medline.

(8) Birbes, H.; El Bawab, S.; Hannun, Y. A.; Obeid, L. M. Selective hydrolysis of a mitochondrial pool of sphingomyelin induces apoptosis. *FASEB J* **2001**, *15* (14), 2669-2679. DOI: 10.1096/fj.01-0539com From NLM Medline.

(9) Mignard, V.; Dubois, N.; Lanoe, D.; Joalland, M. P.; Oliver, L.; Pecqueur, C.; Heymann, D.; Paris, F.; Vallette, F. M.; Lalier, L. Sphingolipid distribution at mitochondria-associated membranes (MAMs) upon induction of apoptosis. *J Lipid Res* **2020**, *61* (7), 1025-1037. DOI: 10.1194/jlr.RA120000628 From NLM Medline.

(10) Zhang, T.; Barclay, L.; Walensky, L. D.; Saghatelian, A. Regulation of mitochondrial ceramide distribution by members of the BCL-2 family. *J Lipid Res* **2015**, *56* (8), 1501-1510. DOI: 10.1194/jlr.M058750 From NLM Medline.

(11) Bourbon, N. A.; Sandirasegarane, L.; Kester, M. Ceramide-induced inhibition of Akt is mediated through protein kinase Czeta: implications for growth arrest. *J Biol Chem* **2002**, *277* (5), 3286-3292. DOI: 10.1074/jbc.M110541200 From NLM Medline.

(12) Dadsena, S.; Bockelmann, S.; Mina, J. G. M.; Hassan, D. G.; Korneev, S.; Razzera, G.; Jahn, H.; Niekamp, P.; Muller, D.; Schneider, M.; et al. Ceramides bind VDAC2 to trigger mitochondrial apoptosis. *Nat Commun* **2019**, *10* (1), 1832. DOI: 10.1038/s41467-019-09654-4 From NLM Medline.

(13) Lizardo, D. Y.; Lin, Y. L.; Gokcumen, O.; Atilla-Gokcumen, G. E. Regulation of lipids is central to replicative senescence. *Mol Biosyst* **2017**, *13* (3), 498-509. DOI: 10.1039/c6mb00842a.

(14) Saitou, M.; Lizardo, D. Y.; Taskent, R. O.; Millner, A.; Gokcumen, O.; Atilla-Gokcumen, G. E. An evolutionary transcriptomics approach links CD36 to membrane remodeling in replicative senescence. *Mol Omics* **2018**, *14* (4), 237-246. DOI: 10.1039/c8mo00099a.

(15) Millner, A.; Lizardo, D. Y.; Atilla-Gokcumen, G. E. Untargeted Lipidomics Highlight the Depletion of Deoxyceramides during Therapy-Induced Senescence. *Proteomics* **2020**, *20* (10), e2000013. DOI: 10.1002/pmic.202000013.
(16) Millner, A.; Running, L.; Colon-Rosa, N.; Aga, D. S.; Frasor, J.; Atilla-Gokcumen, G. E. Ceramide-1-Phosphate Is Involved in Therapy-Induced Senescence. *ACS Chem Biol* **2022**, *17* (4), 822-828. DOI: 10.1021/acschembio.2c00216.
(17) Li, S.; Kim, H. E. Implications of Sphingolipids on Aging and Age-Related Diseases. *Front Aging* **2021**, *2*, 797320. DOI: 10.3389/fragi.2021.797320 From NLM PubMed-not-MEDLINE.
(18) Khayrullin, A.; Krishnan, P.; Martinez-Nater, L.; Mendhe, B.; Fulzele, S.; Liu, Y.; Mattison, J. A.; Hamrick, M. W. Very Long-Chain C24:1 Ceramide Is Increased in Serum Extracellular Vesicles with Aging and Can Induce Senescence in Bone-Derived Mesenchymal Stem Cells. *Cells* **2019**, *8* (1). DOI: 10.3390/cells8010037 From NLM Medline.
(19) Jadhav, K. S.; Dungan, C. M.; Williamson, D. L. Metformin limits ceramide-induced senescence in C2C12 myoblasts. *Mech Ageing Dev* **2013**, *134* (11-12), 548-559. DOI: 10.1016/j.mad.2013.11.002 From NLM Medline.
(20) Granzotto, A.; Bomba, M.; Castelli, V.; Navarra, R.; Massetti, N.; d'Aurora, M.; Onofrj, M.; Cicalini, I.; Del Boccio, P.; Gatta, V.; et al. Inhibition of de novo ceramide biosynthesis affects aging phenotype in an in vitro model of neuronal senescence. *Aging (Albany NY)* **2019**, *11* (16), 6336-6357. DOI: 10.18632/aging.102191 From NLM Medline.
(21) Lizardo, D. Y.; Lin, Y. L.; Gokcumen, O.; Atilla-Gokcumen, G. E. Regulation of lipids is central to replicative senescence. *Mol Biosyst* **2017**, *13* (3), 498-509. DOI: 10.1039/c6mb00842a From NLM Medline.
(22) Zelnik, I. D.; Volpert, G.; Viiri, L. E.; Kauhanen, D.; Arazi, T.; Aalto-Setala, K.; Laaksonen, R.; Futerman, A. H. Different rates of flux through the biosynthetic pathway for long-chain versus very-long-chain sphingolipids. *J Lipid Res* **2020**, *61* (10), 1341-1346. DOI: 10.1194/jlr.RA120000984 From NLM Medline.
(23) Kumagai, K.; Hanada, K. Structure, functions and regulation of CERT, a lipid-transfer protein for the delivery of ceramide at the ER-Golgi membrane contact sites. *FEBS Lett* **2019**, *593* (17), 2366-2377. DOI: 10.1002/1873-3468.13511 From NLM Medline.
(24) Hanada, K.; Sakai, S.; Kumagai, K. Natural Ligand-Mimetic and Nonmimetic Inhibitors of the Ceramide Transport Protein CERT. *Int J Mol Sci* **2022**, *23* (4). DOI: 10.3390/ijms23042098 From NLM Medline.
(25) Pliss, A.; Kuzmin, A. N.; Kachynski, A. V.; Prasad, P. N. Nonlinear optical imaging and Raman microspectrometry of the cell nucleus throughout the cell cycle. *Biophys J* **2010**, *99* (10), 3483-3491. DOI: 10.1016/j.bpj.2010.06.069.
(26) O'Malley, J.; Kumar, R.; Kuzmin, A. N.; Pliss, A.; Yadav, N.; Balachandar, S.; Wang, J.; Attwood, K.; Prasad, P. N.; Chandra, D. Lipid quantification by Raman microspectroscopy as a potential biomarker in prostate cancer. *Cancer Letters* **2017**, *397*, 52-60. DOI: https://doi.org/10.1016/j.canlet.2017.03.025.
(27) Pliss, A.; Kuzmin, A. N.; Lita, A.; Kumar, R.; Celiku, O.; Atilla-Gokcumen, G. E.; Gokcumen, O.; Chandra, D.; Larion, M.; Prasad, P. N. A Single-Organelle Optical Omics Platform for Cell Science and Biomarker Discovery. *Analytical Chemistry* **2021**, *93* (23), 8281-8290. DOI: 10.1021/acs.analchem.1c01131.
(28) Bakthavatsalam, S.; Dodo, K.; Sodeoka, M. A decade of alkyne-tag Raman imaging (ATRI): applications in biological systems. *RSC Chem Biol* **2021**, *2* (5), 1415-1429. DOI: 10.1039/d1cb00116g From NLM PubMed-not-MEDLINE.

(29) Lita, A.; Kuzmin, A. N.; Pliss, A.; Baev, A.; Rzhevskii, A.; Gilbert, M. R.; Larion, M.; Prasad, P. N. Toward Single-Organelle Lipidomics in Live Cells. *Anal Chem* **2019**, *91* (17), 11380-11387. DOI: 10.1021/acs.analchem.9b02663.
(30) Summers, S. A. Ceramides in insulin resistance and lipotoxicity. *Prog Lipid Res* **2006**, *45* (1), 42-72. DOI: 10.1016/j.plipres.2005.11.002 From NLM Medline.
(31) Hannun, Y. A.; Obeid, L. M. Sphingolipids and their metabolism in physiology and disease. *Nat Rev Mol Cell Biol* **2018**, *19* (3), 175-191. DOI: 10.1038/nrm.2017.107 From NLM Medline.
(32) Volmer, R.; Ron, D. Lipid-dependent regulation of the unfolded protein response. *Curr Opin Cell Biol* **2015**, *33*, 67-73. DOI: 10.1016/j.ceb.2014.12.002 From NLM Medline.
(33) Pluquet, O.; Pourtier, A.; Abbadie, C. The unfolded protein response and cellular senescence. A review in the theme: cellular mechanisms of endoplasmic reticulum stress signaling in health and disease. *Am J Physiol Cell Physiol* **2015**, *308* (6), C415-425. DOI: 10.1152/ajpcell.00334.2014 From NLM Medline.
(34) Druelle, C.; Drullion, C.; Desle, J.; Martin, N.; Saas, L.; Cormenier, J.; Malaquin, N.; Huot, L.; Slomianny, C.; Bouali, F.; et al. ATF6alpha regulates morphological changes associated with senescence in human fibroblasts. *Oncotarget* **2016**, *7* (42), 67699-67715. DOI: 10.18632/oncotarget.11505 From NLM Medline.
(35) Cormenier, J.; Martin, N.; Desle, J.; Salazar-Cardozo, C.; Pourtier, A.; Abbadie, C.; Pluquet, O. The ATF6alpha arm of the Unfolded Protein Response mediates replicative senescence in human fibroblasts through a COX2/prostaglandin E(2) intracrine pathway. *Mech Ageing Dev* **2018**, *170*, 82-91. DOI: 10.1016/j.mad.2017.08.003 From NLM Medline.
(36) Obeid, L. M.; Hannun, Y. A. Ceramide, stress, and a "LAG" in aging. *Sci Aging Knowledge Environ* **2003**, *2003* (39), PE27. DOI: 10.1126/sageke.2003.39.pe27 From NLM Medline.
(37) Lindner, P.; Christensen, S. B.; Nissen, P.; Moller, J. V.; Engedal, N. Cell death induced by the ER stressor thapsigargin involves death receptor 5, a non-autophagic function of MAP1LC3B, and distinct contributions from unfolded protein response components. *Cell Commun Signal* **2020**, *18* (1), 12. DOI: 10.1186/s12964-019-0499-z From NLM Medline.
(38) Zelnik, I. D.; Ventura, A. E.; Kim, J. L.; Silva, L. C.; Futerman, A. H. The role of ceramide in regulating endoplasmic reticulum function. *Biochim Biophys Acta Mol Cell Biol Lipids* **2020**, *1865* (1), 158489. DOI: 10.1016/j.bbalip.2019.06.015 From NLM Medline.
(39) Chen, Q.; Kovilakath, A.; Allegood, J.; Thompson, J.; Hu, Y.; Cowart, L. A.; Lesnefsky, E. J. Endoplasmic reticulum stress and mitochondrial dysfunction during aging: Role of sphingolipids. *Biochim Biophys Acta Mol Cell Biol Lipids* **2023**, *1868* (10), 159366. DOI: 10.1016/j.bbalip.2023.159366 From NLM Medline.
(40) Koloko Ngassie, M. L.; Drake, L. Y.; Roos, B. B.; Koenig-Kappes, A.; Pabelick, C. M.; Gosens, R.; Brandsma, C. A.; Burgess, J. K.; Prakash, Y. S. Endoplasmic reticulum stress-induced senescence in human lung fibroblasts. *Am J Physiol Lung Cell Mol Physiol* **2024**, *327* (1), L126-L139. DOI: 10.1152/ajplung.00264.2023 From NLM Medline.

Supplementary Information

ER-Localized Ceramide Accumulation Due to Disrupted CERT Transport Contributes to Replicative Senescence

Shweta Chitkara[1], Natasha Gozali[1], Andrey Kuzmin[1], Artem Pliss[2], Paras Prasad[1], Yasemin Sancak[3], G. Ekin Atilla-Gokcumen[1]*.

[1]Department of Chemistry, University at Buffalo, The State University of New York, Buffalo, New York 14260, USA

[2]School of Pharmacy, D'Youville University, Buffalo, New York 14201

[3] Department of Pharmacology, University of Washington, Seattle, WA

*Corresponding author: ekinatil@buffalo.edu (G. Ekin Atilla-Gokcumen)

Figure S1. (A) This is a representative growth curve for MRC-5 showing the number of days the cells were in culture along with the population doubling that was calculated each time cells were split. The population doubling is calculated using the following formula: $2^n = (P/P_0)$, where P_0 is the number of cells plated, P is the number of cells in the plate before splitting, n is the number of times the cell population increased by two-fold from the time they were plated to the time they were ready to be split. The x-axis at each point on the graph corresponds to the nth day the cells were split. The y-axis represents the population doubling of the cells at each time cells were split. **(B)** Dose-viability data for Dox. MRC-5 cells were plated in a 96-well plate and the cells were treated with varying concentrations of Dox. Cell viability was assessed using MTT assay. *** represents p<0.001, **** represents p<0.0001.

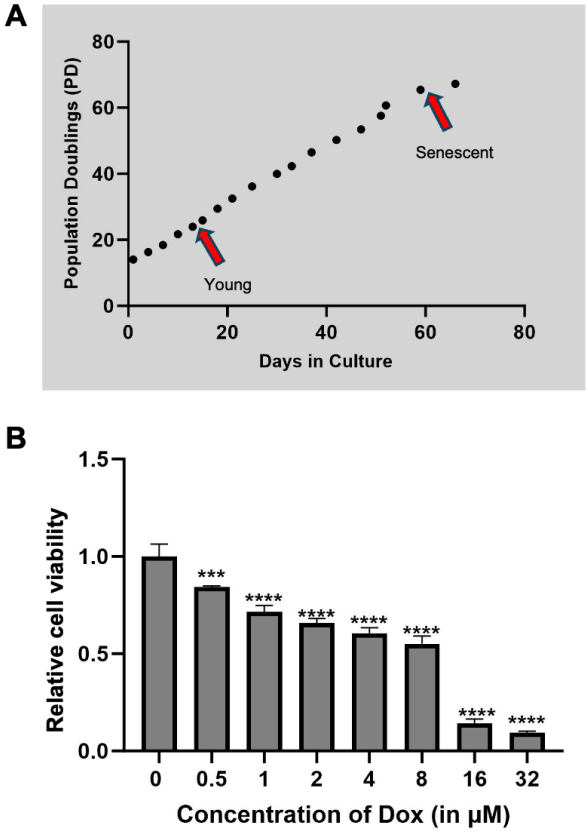

Figure S2. Gene expression of enzymes involved in sphingolipid biosynthesis in replicative senescence and apoptosis. This is a relative gene expression of enzymes in both models of MRC-5, human lung fibroblast cells. The expression of each gene is normalized to a housekeeping reference gene, *HPRT1*. n=3 for senescent cells and n=5 for apoptotic cells. * represents p<0.05, ** represents p<0.001, *** represents p<0.0001, **** represents p<0.00001, ns represents not significant. *SPTLC2*, serine palmitoyl transferase long chain base subunit 2; *KDSR*, 3-ketodihydrosphingosine reductase; *DEGS1*, delta 4-desaturase, sphingolipid 1; *CerS1/2/5/6*, ceramide synthase 1/2/5/6 ; *ASAH1*, N-acylsphingosine amidohydrolase 1; *SGMS1-2*, sphingomyelin synthase 1-2; *CerK*, ceramide kinase; *SMPD1-2*, sphingomyelin phosphodiesterase 1-2; *UGCG*, UDP-glucose ceramide glucosyltransferase; *GBA*, beta-glucocerebrosidase; *SPHK1-2*, sphingosine kinase 1-2; *SGPL1*, sphingosine-1-phosphate lyase 1; *CerT*, ceramide transfer protein.

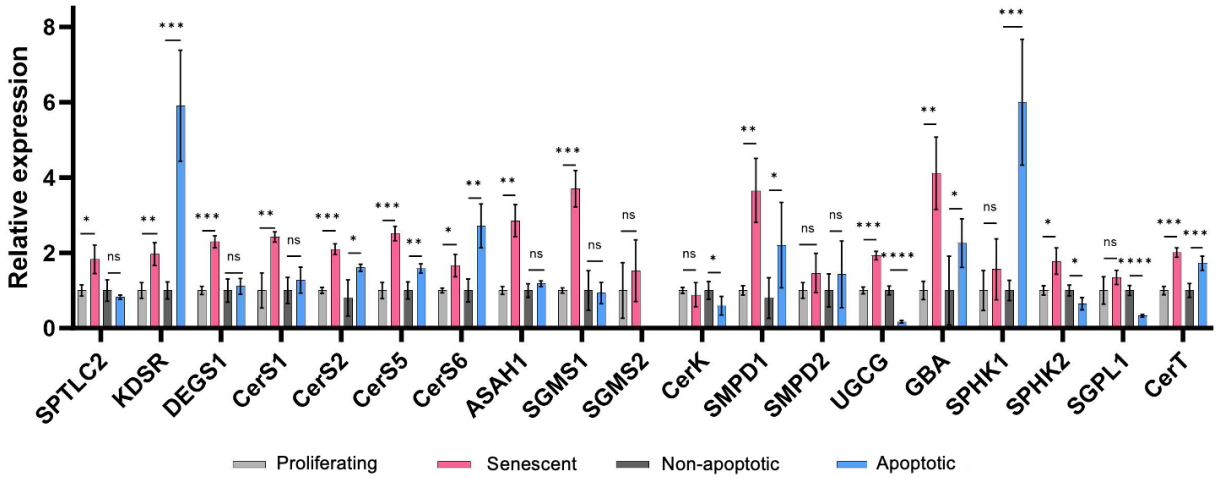

Figure S3. Dose-response profile for HPA12. MTT assay was used to obtain a dose-response curve for HPA12. MRC-5 cells were plated in a 96-well plate and the cells were treated with varying concentrations of HPA12 before performing cell viability assay.

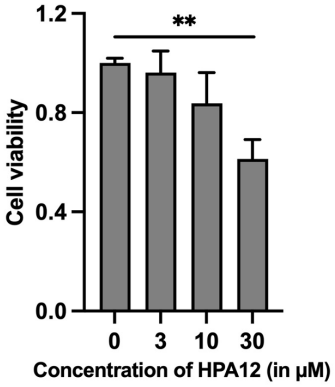

Table S1. Sphingolipid levels in senescent cells w.r.t proliferating cells. n=3 for each condition. m/z is the theoretical mass-to-charge ratio. Fold changes and p-values of the sphingolipid species- ceramide, dihydroceramide, hexosylceramide and sphingomyelin are provided in this table. Fold changes are calculated as **[Abundance$_{\text{senescent cells}}$]/[Abundance$_{\text{proliferating cells}}$]** for each species. Abundance is the total ion count for a given ion. p-value for senescent condition is calculated with respect to the proliferating cells condition.

Species		m/z $_{theo}$	Ions	FC	pvalue
Ceramide	C14:0	508.4730	$[M-H]^-$	1.3	0.1895
	C16:1	534.4892		2.3	0.0189
	C16:0	536.5048		1.8	0.0224
	C18:1	562.5205		1.9	0.0102
	C18:0	564.5361		1.3	0.1739
	C20:0	592.5674		1.5	0.0932
	C22:1	618.5831		1.7	0.0237
	C22:0	620.5987		1.9	0.0107
	C24:1	646.6144		2.1	0.0080
	C24:0	648.6300		2.5	0.0054
	C26:1	674.6456		0.9	0.5724
	C26:0	676.6613		1.1	0.3217
Dihydro-ceramide	C16:0	538.5204	$[M-H]^-$	1.2	0.1733
	C18:0	566.5517		1.1	0.3909
	C20:0	594.5830		0.9	0.2944
	C22:0	622.6143		1.3	0.0837
Hexosyl-ceramide	C16:1	696.5420	$[M-H]^-$	1.2	0.3424
	C16:0	698.5576		0.9	0.7287
	C18:1	724.5733		1.2	0.2666
	C18:0	726.5889		1.4	0.1453
	C20:1	752.6045		1.3	0.2184
	C20:0	754.6202		1.4	0.1735
	C22:0	782.6515		1.7	0.0339
Sphingomyelin	C14:1	673.5279	$[M+H]^+$	0.5	0.0064
	C14:0	675.5436		0.4	0.0000
	C16:1	701.5592		0.6	0.0029
	C16:0	703.5749		0.7	0.0025
	C18:1	729.5905		0.3	0.0016
	C18:0	731.6062		0.9	0.3051
	C22:0	787.6688		0.7	0.0017
	C24:1	813.6844		0.5	0.0007
	C24:0	815.7001		0.8	0.0313
	C26:1	841.7157		0.4	0.0005
	C26:0	843.7314		0.5	0.0079

Table S2. Sphingolipid levels in apoptotic cells w.r.t control cells. n=3 for each condition. m/z is the theoretical mass-to-charge ratio. Fold changes and p-values of the sphingolipid species- ceramide, hexosylceramide and sphingomyelin are provided in this table. Fold changes are calculated as **[Abundance$_{\text{apoptotic cells}}$]/[Abundance$_{\text{control cells}}$]** for each species. Abundance is the total ion count for a given ion. p-value for apoptotic condition is calculated with respect to the control.

Species		m/z $_{theo}$	Ions	FC	pvalue
Ceramide	C14:0	508.4730	$[M-H]^-$	2.0	0.0013
	C16:1	534.4892		3.8	0.0020
	C16:0	536.5048		2.3	0.0028
	C18:1	562.5205		2.7	0.0013
	C18:0	564.5361		2.3	0.0121
	C20:0	592.5674		1.8	0.0599
	C22:1	618.5831		2.4	0.0015
	C22:0	620.5987		2.1	0.0221
	C24:1	646.6144		2.0	0.0007
	C24:0	648.6300		2.0	0.0590
	C26:1	674.6456		1.2	0.5404
	C26:0	676.6613		1.6	0.1255
Hexosyl-ceramide	C16:0	698.5576	[M-H]-	0.8	0.2535
	C18:1	724.5733		1.8	0.0045
	C18:0	726.5889		2.2	0.0001
	C22:0	782.6515		1.0	0.9406
	C24:1	808.6672		0.8	0.2057
	C24:0	810.6828		1.2	0.3711
Sphingomyelin	C14:0	675.5436	$[M+H]^+$	1.6	0.1387
	C16:1	701.5592		1.4	0.2712
	C16:0	703.5749		1.7	0.1117
	C18:0	731.6062		2.3	0.0721
	C24:0	815.7001		2.3	0.0752
	C24:1	813.6844		1.6	0.1212
	C26:1	841.7157		0.9	0.6182

Table S3. Sequences of primers used for droplet digital PCR

Gene	Description	Forward primer	Reverse primer	Exon
SPTLC2	Serine palmitoyltransferase 2	GAAATCCAACCACAACGACAC	AATGAAGACTCTCCAGTAGTGC	10 to 11
KDSR	3-Ketodihydrosphingosine Reductase	CATGGTGTCTCCGCTCATC	AGCTCCTTGTTTATAGCACTCG	1 to 2c
DEGS1	Delta 4-Desaturase, Sphingolipid 1	TGTAGTGAGGGAGGTTGTCAT	TTACTCATATTATGGGCCTCTGAA	2 to 3
CerS1	Ceramide Synthase 1	GCCTTCCACAACCTCCTG	AACTGGGTAACAAGCAGAGTC	6b to 6b
CerS2	Ceramide Synthase 2	CACTGCGTTCATCTTCTACCA	GCTCTATCCTGCCTTCTTTGG	10 to 11
CerS5	Ceramide Synthase 5	CCGATTATCTCCCAACTCTCAA	GCCAATTATGCCAAGTATCAGC	8 to 9
CerS6	Ceramide Synthase 6	TGACTCCGTAGGTAAATACATAAAGG	CAATCAGGAGAAGCCAAGCA	3 to 4
ASAH1	Acid ceramidase	GCCAGTTATGACCCAGGTATC	TGTACTTCAATAGTAGCAGAAGACA	8 to 10
SGMS1	Sphingomyelin synthase 1	GTACAGATAGTCCCCACACAT	GCATTTCAACTGTTCTCCGAAG	8 to 9
SGMS2	Sphingomyelin synthase 2	TGCTGTACCTTCACCACTTTC	GGTCTTTCTCATCCTGCTGT	3b to 4
CerK	Ceramide kinase	CACCTCGCTGAACATACCATC	ACCACTGTTCACCTTAGCC	4 to 6
SMPD1	Sphingomyelin phosphodiesterase 1	5'-GAGAGAGATGAGGCGGAGA-3'	5'-CTGGCTCTATGAAGCGATGG-3	2 to 3
SMPD2	Sphingomyelin phosphodiesterase 2	GGATCTTCAACCTCAACTGCT	GAAGTCCTGCTCACTCCA	1 to 3
UGCG	Ceramide glucosyltransferase	GCATTGCAACTTGAGTGGAC	GATGTGTTGGATCAAGCAGGA	6 to 7
GBA	Glucosylceramidase beta 1	TTCGTTTTGCCTCCGGTT	AGAGTCTCTGAAGGAATCGAGGAT	1 to 2c
SPHK1	Sphingosine kinase 1	TTCACGCTGATGCTCACTG	CCGTTCACCACCTCGTG	3 to 5
SPHK2	Sphingosine kinase 2	CCTTCAACCTCATCCAGACAG	CCCGTTCAGCACCTCAT	5 to 7
SGPL1	Sphingosine-1-phosphate lyase 1	ATATGAGTTTGTCTTCCAGCCA	CTTGGTCTTGTTCAACTTGTCTTG	6 to 7
CerT	Ceramide transfer protein	CCTGAGCACGAAGATACCAAA	TGAAGATGAAACAGAGTATGGCT	3 to 4
HPRT1	Hypoxanthine Phosphoribosyltransferase 1	GTATTCATTATAGTCAAGGGCATATCC	AGATGGTCAAGGTCGCAAG	6 to 8

Table S4. Sphingolipid levels in HPA12-treated cells w.r.t control cells. n=3 for each condition. m/z is the theoretical mass-to-charge ratio. Fold changes and p-values of the sphingolipid species- ceramide, hexosylceramide and sphingomyelin are provided in this table. Fold changes are calculated as **[Abundance$_{inhibitor\text{-}treated}$]/[Abundance$_{control}$]** for each species. Abundance is the total ion count for a given ion. p-value for inhibitor-treated condition is calculated with respect to the control.

Species		m/z	IONS	HPA12 (3 μM)		HPA12 (10 μM)	
				FC	p-value	FC	p-value
Ceramide	C14:0	508.4730	$[M-H]^-$	0.9	0.2249	0.9	0.6485
	C16:0	536.5048		0.8	0.2195	0.9	0.4735
	C18:1	562.5205		1.0	0.8817	1.1	0.5175
	C20:0	592.5674		1.0	0.9301	0.9	0.5840
	C22:0	620.5987		0.7	0.0923	0.6	0.0733
	C24:1	646.6144		0.7	0.0989	0.6	0.0914
	C24:0	648.6300		0.6	0.0281	0.4	0.0210
	C26:1	674.6456		0.4	0.0013	0.4	0.0036
Hexosyl-ceramide	C16:0	698.5576	$[M-H]^-$	1.5	0.0342	1.6	0.0149
	C22:0	782.6515		1.2	0.2200	1.3	0.0850
Sphingomyelin	C14:0	675.5436	$[M+H]^+$	1.6	0.0412	1.0	0.9372
	C16:0	703.5749		0.4	0.0038	0.2	0.0016
	C18:1	729.5905		0.6	0.0193	0.4	0.0061
	C22:0	787.6688		0.2	0.0044	0.1	0.0028
	C24:1	813.6844		0.2	0.0034	0.2	0.0026
	C24:0	815.7001		0.2	0.0044	0.1	0.0030